Improved Limit on Neutrinoless Double-Beta Decay in ^{130} Te with CUORE

Improved Limit on Neutrinoless Double-Beta Decay in ^{130}Te with CUORE

D. Q. Adams,[1] C. Alduino,[1] K. Alfonso,[2] F. T. Avignone III,[1] O. Azzolini,[3] G. Bari,[4] F. Bellini,[5,6]
G. Benato,[7,8] M. Biassoni,[9] A. Branca,[10,9] C. Brofferio,[10,9] C. Bucci,[8] A. Caminata,[11] A. Campani,[12,11]
L. Canonica,[13,8] X. G. Cao,[14] S. Capelli,[10,9] L. Cappelli,[8,7,15] L. Cardani,[6] P. Carniti,[10,9] N. Casali,[6]
D. Chiesa,[10,9] N. Chott,[1] M. Clemenza,[10,9] S. Copello,[16,8] C. Cosmelli,[5,6] O. Cremonesi,[9,a] R. J. Creswick,[1]
A. D'Addabbo,[8] D. D'Aguanno,[8,17] I. Dafinei,[6] C. J. Davis,[18] S. Dell'Oro,[19] S. Di Domizio,[12,11] V. Dompè,[8,16]
D. Q. Fang,[14] G. Fantini,[8,16] M. Faverzani,[10,9] E. Ferri,[10,9] F. Ferroni,[16,6] E. Fiorini,[9,10] M. A. Franceschi,[20]
S. J. Freedman,[15,7,b] B. K. Fujikawa,[15] A. Giachero,[10,9] L. Gironi,[10,9] A. Giuliani,[21] P. Gorla,[8] C. Gotti,[10,9]
T. D. Gutierrez,[22] K. Han,[23] K. M. Heeger,[18] R. G. Huang,[7] H. Z. Huang,[2] J. Johnston,[13] G. Keppel,[3]
Yu. G. Kolomensky,[7,15] C. Ligi,[20] Y. G. Ma,[14] L. Ma,[2] L. Marini,[7,15] R. H. Maruyama,[18] Y. Mei,[15]
N. Moggi,[24,4] S. Morganti,[6] T. Napolitano,[20] M. Nastasi,[10,9] J. Nikkel,[18] C. Nones,[25] E. B. Norman,[26,27]
V. Novati,[28] A. Nucciotti,[10,9] I. Nutini,[10,9] T. O'Donnell,[19] J. L. Ouellet,[13] C. E. Pagliarone,[8,17]
L. Pagnanini,[10,9] M. Pallavicini,[12,11] L. Pattavina,[8] M. Pavan,[10,9] G. Pessina,[9] V. Pettinacci,[6] C. Pira,[3]
S. Pirro,[8] S. Pozzi,[10,9] E. Previtali,[9,10] A. Puiu,[10,9] C. Rosenfeld,[1] C. Rusconi,[1,8] M. Sakai,[7] S. Sangiorgio,[26]
B. Schmidt,[15] N. D. Scielzo,[26] V. Sharma,[19] V. Singh,[7] M. Sisti,[10,9] D. Speller,[18] P. T. Surukuchi,[18]
L. Taffarello,[29] F. Terranova,[10,9] C. Tomei,[6] M. Vignati,[6] S. L. Wagaarachchi,[7,15] B. S. Wang,[26,27]
B. Welliver,[15] J. Wilson,[1] K. Wilson,[1] L. A. Winslow,[13] L. Zanotti,[10,9] S. Zimmermann,[30] and S. Zucchelli[24,4]

(CUORE Collaboration)

[1]*Department of Physics and Astronomy, University of South Carolina, Columbia, SC 29208, USA*
[2]*Department of Physics and Astronomy, University of California, Los Angeles, CA 90095, USA*
[3]*INFN – Laboratori Nazionali di Legnaro, Legnaro (Padova) I-35020, Italy*
[4]*INFN – Sezione di Bologna, Bologna I-40127, Italy*
[5]*Dipartimento di Fisica, Sapienza Università di Roma, Roma I-00185, Italy*
[6]*INFN – Sezione di Roma, Roma I-00185, Italy*
[7]*Department of Physics, University of California, Berkeley, CA 94720, USA*
[8]*INFN – Laboratori Nazionali del Gran Sasso, Assergi (L'Aquila) I-67100, Italy*
[9]*INFN – Sezione di Milano Bicocca, Milano I-20126, Italy*
[10]*Dipartimento di Fisica, Università di Milano-Bicocca, Milano I-20126, Italy*
[11]*INFN – Sezione di Genova, Genova I-16146, Italy*
[12]*Dipartimento di Fisica, Università di Genova, Genova I-16146, Italy*
[13]*Massachusetts Institute of Technology, Cambridge, MA 02139, USA*
[14]*Key Laboratory of Nuclear Physics and Ion-Beam Application (MOE),*
Institute of Modern Physics, Fudan University, Shanghai 200433, China
[15]*Nuclear Science Division, Lawrence Berkeley National Laboratory, Berkeley, CA 94720, USA*
[16]*Gran Sasso Science Institute, L'Aquila I-67100, Italy*
[17]*Dipartimento di Ingegneria Civile e Meccanica,*
Università degli Studi di Cassino e del Lazio Meridionale, Cassino I-03043, Italy
[18]*Wright Laboratory, Department of Physics, Yale University, New Haven, CT 06520, USA*
[19]*Center for Neutrino Physics, Virginia Polytechnic Institute and State University, Blacksburg, Virginia 24061, USA*
[20]*INFN – Laboratori Nazionali di Frascati, Frascati (Roma) I-00044, Italy*
[21]*CSNSM, Univ. Paris-Sud, CNRS/IN2P3, Université Paris-Saclay, 91405 Orsay, France*
[22]*Physics Department, California Polytechnic State University, San Luis Obispo, CA 93407, USA*
[23]*INPAC and School of Physics and Astronomy,*
Shanghai Jiao Tong University; Shanghai Laboratory for Particle Physics and Cosmology, Shanghai 200240, China
[24]*Dipartimento di Fisica e Astronomia, Alma Mater Studiorum – Università di Bologna, Bologna I-40127, Italy*
[25]*Service de Physique des Particules, CEA / Saclay, 91191 Gif-sur-Yvette, France*
[26]*Lawrence Livermore National Laboratory, Livermore, CA 94550, USA*
[27]*Department of Nuclear Engineering, University of California, Berkeley, CA 94720, USA*
[28]*CSNSM, Univ. Paris-Sud, CNRS/IN2P3, Universit Paris-Saclay, 91405 Orsay, France*
[29]*INFN – Sezione di Padova, Padova I-35131, Italy*
[30]*Engineering Division, Lawrence Berkeley National Laboratory, Berkeley, CA 94720, USA*
(Dated: March 2, 2020)

We report new results from the search for neutrinoless double-beta decay in ^{130}Te with the CUORE detector. This search benefits from a four-fold increase in exposure, lower trigger thresholds and analysis improvements relative to our previous results. We observe a background of $(1.38 \pm 0.07) \cdot 10^{-2}$ counts/(keV·kg·yr) in the $0\nu\beta\beta$ decay region of interest and, with a total exposure of 372.5 kg·yr, we attain a median exclusion sensitivity of $1.7 \cdot 10^{25}$ yr. We find no evidence for $0\nu\beta\beta$

decay and set a 90% CI Bayesian lower limit of $3.2 \cdot 10^{25}$ yr on the ^{130}Te half-life for this process. In the hypothesis that $0\nu\beta\beta$ decay is mediated by light Majorana neutrinos, this results in an upper limit on the effective Majorana mass of 75–350 meV, depending on the nuclear matrix elements used.

The search for neutrinoless double-beta ($0\nu\beta\beta$) decay is one of the top priorities in nuclear and astroparticle physics. If observed, this process would unambiguously demonstrate that lepton number is not a conserved quantity, and the Majorana nature of neutrinos [1–4]. This matter-creating process could provide corroborating evidence for the leptogenesis explanation of the baryon asymmetry of the universe [5], and would imply a new mechanism for generating neutrino masses. In the simplest scenario whereby $0\nu\beta\beta$ decay is mediated by the exchange of a light Majorana neutrino, the rate of the process depends on the effective Majorana mass $m_{\beta\beta}$, though other scenarios exist [6–13]. Even in the absence of direct observation, constraints on the $0\nu\beta\beta$ decay rate can provide important information on the scale, ordering and origin of neutrino masses [14].

Since the $0\nu\beta\beta$ decay involves a transition from a nucleus with (Z, N) protons and neutrons to $(Z+2, N-2)$ with the emission of two electrons and no neutrinos, the signature is a peak in the summed energy spectrum of the final-state electrons at the end point of the two neutrino double-beta decay spectrum ($Q_{\beta\beta}$). A discovery of the process requires low backgrounds near $Q_{\beta\beta}$, large masses of isotope, and good energy resolution. A wide range of detector technologies is employed in the worldwide search for $0\nu\beta\beta$ decay across a number of isotopes. The current generation experiments probe half-life values between $10^{25} - 10^{26}$ yr corresponding to $m_{\beta\beta}$ $\mathcal{O}(100\,\text{meV})$ [15–19]. The next generation experiments are planning to instrument $\mathcal{O}(1000\,\text{kg})$ of isotope and be sensitive to half-lives beyond 10^{27} yr [14].

CUORE [20, 21] is a ton-scale cryogenic detector located at Laboratori Nazionali del Gran Sasso (LNGS) in Italy searching for $0\nu\beta\beta$ decay in ^{130}Te. The experiment consists of an array of 988 TeO$_2$ crystals operating as cryogenic calorimeters [22–24] – also denoted as bolometers – at a temperature of about 10 mK. The detector features excellent energy resolution of < 10 keV FWHM in the $0\nu\beta\beta$ region of interest (ROI), large detection efficiency, and low background. CUORE chose ^{130}Te because of its high $Q_{\beta\beta} = (2527.518 \pm 0.013)$ keV [25–27] – above most of the natural radioactive background – and isotopic abundance of $(34.167 \pm 0.002)\%$ [28], which allows cost-effective use of natural tellurium. CUORE is the culmination of decades of development of large-scale bolometric detectors [29–33] and its successful operation demonstrates the high potential of this technology.

The CUORE crystals are cubes of $5 \times 5 \times 5$ cm^3 and mass of 750 g [31], arranged in 19 towers. Each crystal is instrumented with a neutron-transmutation-doped (NTD) germanium thermistor [34] to record thermal pulses, and a silicon heater [35, 36] that provides reference pulses for thermal gain stabilization. The detector is housed in a state-of-the-art cryostat, which shields the detectors from both thermal and gamma radiation. Cooling at the 10 mK stage is achieved by a custom ^{3}He/^{4}He dilution refrigerator [24, 37–43].

In this letter, we present an analysis of the data collected between May 2017 and July 2019, including a re-analysis of data already published [44]. The data are collected in runs of about one day duration, and grouped into datasets which cover roughly a month. Each dataset consists of $0\nu\beta\beta$ decay search (physics) data bracketed by a few days of calibration data collected at the beginning and end. The calibration is performed with either internal ^{232}Th sources [45] or external mixed ^{232}Th-^{60}Co sources, with consecutive datasets sharing the intermediate calibration. Typically, a few days per dataset are devoted to diagnostics and detector validation measurements, such as noise optimization [43], working point configuration, and energy threshold measurements.

Since we began taking data, there have been two major interruptions of the physics data collection due to important maintenance of the cryogenic system, as shown in Fig. 1. After the 2017 data campaign [44], we performed a few modifications to improve the stability and uniformity of the data collection: we decreased the cryostat operating temperature from 15 mK to 11.8 mK, which improves signal-to-noise ratio for injected heater events, and installed an external calibration system, which has a comparable performance to the inner detector calibration system but is less invasive to deploy. During the second interruption in fall 2018 we improved the stability of the cryostat and increased the live-time fraction. Since spring 2019, CUORE has been stably collecting data at an average rate of 50 kg·yr/month.

In this letter, we present an analysis of a 372.5 kg·yr TeO$_2$ exposure from the first 7 datasets, corresponding to 103.6 kg·yr of ^{130}Te exposure – a 4-fold increase in exposure compared to Ref. [44]. The main difference with respect to the first data release is the trigger algorithm. The CUORE data acquisition system [41] saves the full continuous data stream, giving the possibility of digitally retriggering the continuous data samples offline. In this analysis, we use a trigger algorithm based on the optimum filter (OF) [46] which optimizes the signal-to-noise ratio and yields trigger thresholds a few times the detector baseline RMS [47]. The algorithm identifies a signal if the amplitude of the optimum filtered waveform exceeds a threshold automatically determined by the baseline resolution of each calorimeter for each dataset. Figure 2 shows the energy thresholds, at 90% trigger efficiency,
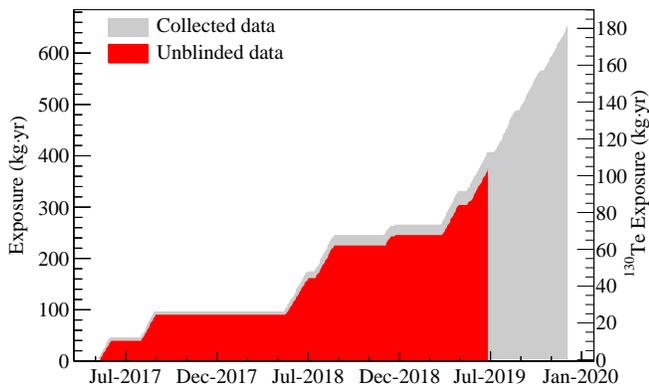
FIG. 1. Exposure collected by CUORE starting from May 2017: the data in gray represent the exposure accumulated at the time of writing, while the data in red are used for the present work (372.5 kg·yr).

obtained with the previously used algorithm, denoted derivative trigger (DT), and the optimum trigger (OT). The OT allows us to lower the energy thresholds by a factor 2–10 with respect to the DT. We set the analysis threshold to 40 keV to minimize the background contribution in the ROI from the 2615 keV [208]Tl line, while at the same time preserving a > 90% trigger efficiency for the majority (>97%) of the calorimeters.
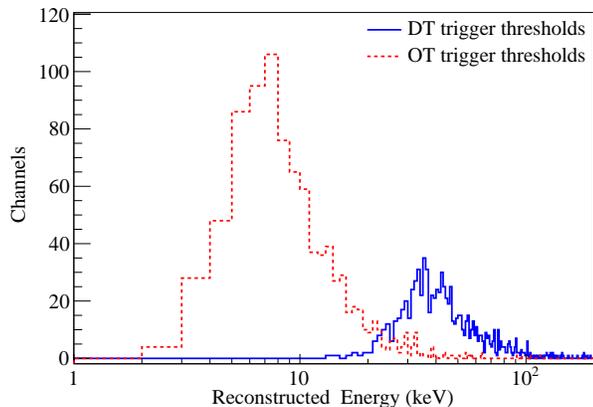

FIG. 2. Distribution of energy thresholds at 90% trigger efficiency for the DT and OT algorithms.

The analysis presented here is divided in three parts: event reconstruction, detector response characterization, and statistical $0\nu\beta\beta$ decay analysis. The goal of the event reconstruction is to extract physical quantities from each 10 s long signal waveform. For each calorimeter and dataset, we build the OF transfer function starting from the average noise power spectrum and the average signal obtained from selected calibration events with minimum energies also tuned for each calorimeter and dataset, and always above 100 keV. For each triggered event, we use the waveform filtered with the OF to evaluate the signal

amplitude. To monitor the thermal response of the detector we use injected heater pulses [48], and correct the amplitudes of signal events for small temperature drifts. A second procedure for thermal gain correction utilizes the [208]Tl events at 2615 keV from calibration data. This is the default method for the calorimeters with an unstable pulser, or not instrumented with a heater.

We use the data acquired in calibration runs to map the stabilized amplitudes to energy values, and select the stabilization procedure which yields the best energy resolution. From Monte Carlo (MC) simulations, in 88% of cases, we expect $0\nu\beta\beta$ decay events to release energy in just one crystal [49]. Hence, we apply an anticoincidence cut by computing the number of calorimeters with a > 40 keV energy deposition within a ±5 ms time window, and keep only events with a single energy deposition for the $0\nu\beta\beta$ decay analysis. We apply a pulse shape analysis (PSA) to reject events with nonphysical or noisy waveforms, and pileup – i.e. superimposed – events. We use a set of six pulse shape parameters to compute the Mahalanobis distance [50] from the mean value of a reference sample of clean events from a physical γ line. We tune our cut on the Mahalanobis distance on a per-dataset basis to optimize the sensitivity to $0\nu\beta\beta$ decay events [44] (see Fig. 3). The PSA cut mostly affects the continuum regions, without impacting the γ and α lines. To avoid a human induced bias in the result, we salt the ROI by moving a random fraction of events in the $[2615 \pm 25]$ keV region into the $[Q_{\beta\beta} \pm 25]$ keV region, and vice versa [44, 49]. The salting is reversed once the analysis procedures are finalized.

The signal efficiency is calculated as the product of the containment efficiency, the trigger and reconstruction efficiency, the anticoincidence efficiency, and the PSA efficiency. We compute the probability that the full energy of $0\nu\beta\beta$ decay is contained in a single crystal using MC simulations. We use the injected heater pulses to evaluate the efficiency of correctly triggering all injected events, reconstructing their pulse energy [44], as well as the probability of false positives in the identification of pileup events. Given the large number of heater events, the trigger, energy reconstruction and pileup rejection efficiencies are obtained for each calorimeter and dataset separately, then averaged over the entire dataset.

We extract the anticoincidence efficiency as the survival probability of the 1460 keV γ line from [40]K in the physics data. This γ line follows an electron capture with a K-shell energy of ~ 3 keV, well below threshold; thus a fully absorbed 1460 keV [40]K γ line is uncorrelated to any other event. Finally, we compute the PSA efficiency by calculating the survival probability of two samples of physical events: double-crystal events whose sum energy is compatible with γ lines, or single crystal events corresponding to fully absorbed γ lines. The former method utilizes events at all energies, since only the summed energy is fixed, and provides a cleaner but smaller data

sample. The latter method profits from higher statistics for most γ lines, but it requires background substraction and only allows for an efficiency determination at a handful of energies. We choose the PSA efficiency as the average of the efficiencies obtained from these two samples ($92.6 \pm 0.1\,\%$) and treat the difference between them as a systematic effect, adding a scaling parameter common to all datasets in the final fit ($\pm 0.7\%$). Given the limited statistics of the physics data, the anticoincidence and PSA efficiencies can only be extracted for an entire dataset, and have larger uncertainties than the efficiencies obtained from heater data. The exposure-weighted average efficiencies are reported in Tab. I.
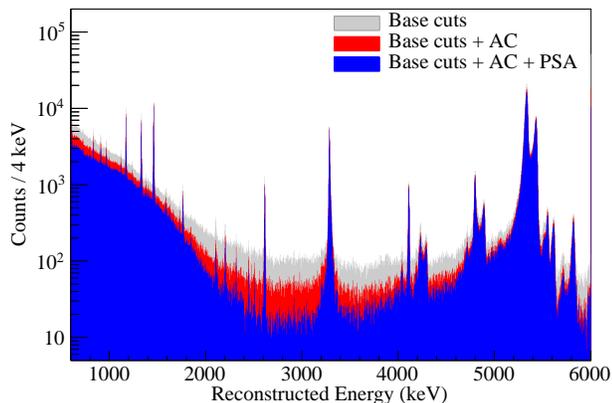

FIG. 3. The CUORE spectrum after applying the base cuts to remove heater events and periods affected by baseline or noise instabilities (gray), after the anticoincidence cut (red), and after the PSA cut (blue).

We extract the detector response function in the ROI for each calorimeter in each dataset by fitting the $2615\,\mathrm{keV}$ ^{208}Tl line in the calibration spectrum [51, 52]. To evaluate possible systematic shifts in the energy scale and the energy dependence of the detector energy resolution, we use the detector response function obtained from the ^{208}Tl calibration peak, with the addition of a linear function to model the background, to fit the 5–7 most prominent γ lines of the physics spectrum. We keep as free parameters the peak position, the peak amplitude, and the ratio of the energy resolution in physics and calibration data. We extract the energy calibration bias – defined as the difference between the reconstructed peak position and its nominal value – and energy resolution, parameterize them quadratically as a function of energy, and interpolate them to $Q_{\beta\beta}$. The exposure-weighted harmonic average of the energy resolution at $Q_{\beta\beta}$ in the physics data is $7.0 \pm 0.4\,\mathrm{keV}$, while the energy bias is $\leq 0.7\,\mathrm{keV}$. A summary of relevant quantities for the $0\nu\beta\beta$ decay analysis is given in Tab. I.

The CUORE physics spectrum (Fig. 4) around $Q_{\beta\beta}$ features a flat distribution with $\sim 90\%$ of the events coming from degraded α particles, as obtained by ex-

TABLE I. Relevant quantities and effective parameters of the analysis. The FWHM of calibration data is the exposure weighted harmonic average over all calorimeters and datasets, which is projected to $Q_{\beta\beta}$ in the physics data. The containment efficiency is from MC simulations, while all other efficiencies correspond to the exposure weighted means.

Number of datasets	7
Number of valid calorimeters (min–max)	900–954
TeO$_2$ exposure	$372.5\,\mathrm{kg \cdot yr}$
FWHM at $2615\,\mathrm{keV}$ in calibration data	$7.73(3)\,\mathrm{keV}$
FWHM at $Q_{\beta\beta}$ in physics data	$7.0(4)\,\mathrm{keV}$
Reconstruction efficiency	$95.802(3)\,\%$
Anticoincidence efficiency	$98.7(1)\,\%$
PSA efficiency	$92.6(1)\,\%$
Total analysis efficiency	$87.5(2)\,\%$
Containment efficiency	$88.35(9)\,\%$ [49]

trapolating from the flat α background in the energy region above the $2615\,\mathrm{keV}$ ^{208}Tl line, and $\sim 10\%$ from $2615\,\mathrm{keV}$ γ events undergoing multiple Compton scattering [53, 54]. The closest expected peak to $Q_{\beta\beta}$ is the ^{60}Co sum peak at $2505.7\,\mathrm{keV}$. We find an additional structure with a significance of $\gtrsim 2\,\sigma$ at $\sim 2480\,\mathrm{keV}$, visible only in the single-crystal spectrum. Its energy corresponds to a ^{60}Co sum peak, with an escaping Te xray, but its amplitude is much larger than expected from MC simulations, and it is not visible in ^{60}Co calibration spectra. We considered various possible contamination, but none justifies the presence of a peak at $\sim 2480\,\mathrm{keV}$ with the observed rate. Thus, more data are needed to assess the significance of this feature. As a consequence, we restrict the fit range to [2490,2575] keV region, and fit the data with a flat background plus peaks described by the detector response function for the ^{60}Co sum line and the potential $0\nu\beta\beta$ decay signal.

We perform an unbinned Bayesian fit combined over all datasets using the BAT software package [55]. The model parameters are the $0\nu\beta\beta$ decay rate ($\Gamma_{0\nu}$), a dataset dependent background index (BI) in counts/(keV·kg·yr), the ^{60}Co sum peak amplitude ($R_{^{60}\mathrm{Co}}$) in counts/(kg·yr), and its position $\mu_{^{60}\mathrm{Co}}$, which is a free parameter as in the previous analysis [44]. The BIs are dataset dependent, while all other parameters are common to all datasets, including the ^{60}Co rate, which is scaled by a dataset dependent factor to account for its decay. We use flat priors for all of the parameters, and restrict the range of the BIs and all peak rates to the physical range, i.e. non-negative values.

We find no evidence for $0\nu\beta\beta$ decay, obtaining the $\Gamma_{0\nu}$ posterior distribution reported in Fig. 5, and a limit of $T_{1/2}^{0\nu} > 3.2 \cdot 10^{25}$ yr at 90% credibility interval (CI), corresponding to the blue dashed curve in Fig. 4. Repeating the fit without the $0\nu\beta\beta$ decay contribution, we obtain an average BI of $(1.38 \pm 0.07) \cdot 10^{-2}$ counts/(keV·kg·yr).

To compute the exclusion sensitivity, we generate 10^4 sets of pseudo-experiments populated with only the ^{60}Co
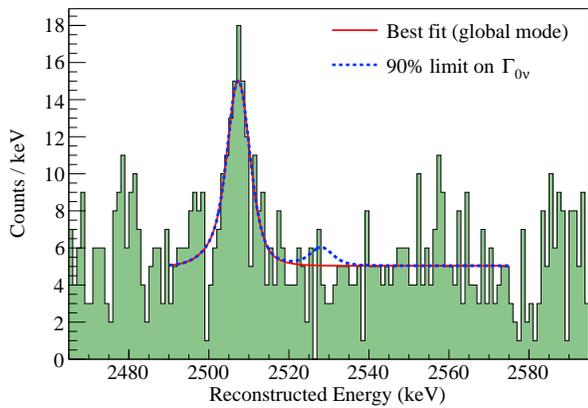
FIG. 4. ROI spectrum with the best-fit curve (solid red) and the best fit-curve with the $0\nu\beta\beta$ decay component fixed to the 90% CI limit (dashed blue).
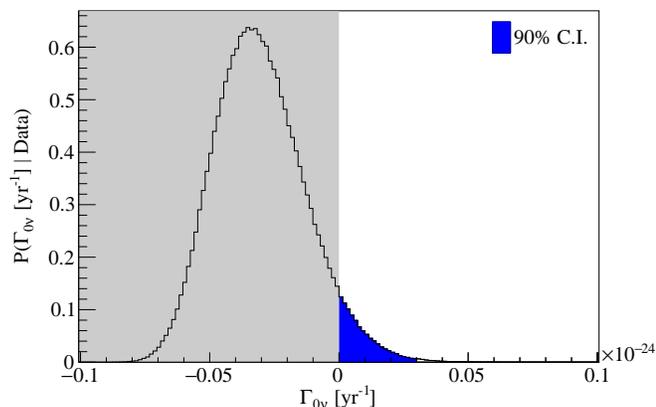

FIG. 5. Posterior on $\Gamma_{0\nu}$ with all systematics included for the fit on the physical range ($\Gamma_{0\nu} > 0$) and on the full range. The 90% CI is shown in blue.

and flat background components, and divided into 7 datasets with the same exposure and BI of the actual datasets as obtained from fitting the data with the background-only model. We fit each pseudo-experiment with the standard signal-plus-background model and obtain a median 90% CI exclusion sensitivity of $1.7 \cdot 10^{25}$ yr. The probability of obtaining a stronger limit than $3.2 \cdot 10^{25}$ yr is 3%.

We consider the following systematic effects. The dominant one is the systematic error on the PSA efficiency. Subdominant effects are induced by the uncertainties on the energy scale, energy resolution, analysis and containment efficiencies, the value of $Q_{\beta\beta}$, and the ^{130}Te natural isotopic abundance. We implement all systematics as additional nuisance parameters in the fit, which can be activated independently, with the priors reported in Tab. II. We evaluate the bias induced by each nuisance parameter by looking at the effect on $\Gamma_{0\nu}$ at the posterior global mode, $\hat{\Gamma}_{0\nu}$; for this, we artificially release the $\Gamma_{0\nu} \geq 0$ constraint, allowing $\Gamma_{0\nu}$ to be negative. The best fit with the

artificially extended range is $\hat{\Gamma}_{0\nu} = (-3.5^{+2.2}_{-1.1}) \cdot 10^{-26}$ yr^{-1}, with a $\sim 1.6\,\sigma$ background under-fluctuation compatible with the p-value quoted above. The inclusion of the additional nuisance parameters affects the global mode on $\Gamma_{0\nu}$ by $\leq 0.04\%$ (see also Tab. II), and yields a 0.4% weaker limit.

Assuming $0\nu\beta\beta$ decay is mediated by light neutrino exchange, and using the phase space factor from Ref. [56], the result above corresponds to a set of upper limits on the effective Majorana mass ranging between 75 and 350 meV, where the spread reflects the different nuclear matrix element calculations available in literature [57–67]. Recent theoretical works [68, 69] show that the inclusion of a contact operator could significantly affect the limit on $m_{\beta\beta}$. The results reported in this paper represent the most stringent limit on $0\nu\beta\beta$ decay in ^{130}Te, and our limit on $m_{\beta\beta}$ is competitive with the leading ones in the field [15–19].

TABLE II. Systematics affecting the $0\nu\beta\beta$ decay analysis. Total analysis efficiency I corresponds to the product of all efficiency terms reported in Tab I, while total analysis efficiency II corresponds to the additional systematic on the PSA efficiency. We report the systematic on the $\Gamma_{0\nu}$ global mode obtained leaving $\Gamma_{0\nu}$ free to assume negative (nonphysical) values.

Fit parameter systematics		
Systematic	Prior	Effect on $\hat{\Gamma}_{0\nu}$
Total analysis efficiency I	Gaussian	0.01%
Total analysis efficiency II	Uniform	0.04%
Containment efficiency	Gaussian	0.01%
Energy and resolution scaling	Multivariate	0.02%
$Q_{\beta\beta}$	Gaussian	0.02%
Isotopic fraction	Gaussian	0.02%

After a period of detector maintenance and optimization, CUORE is stably collecting data at a rate of 50 kg·yr/month. The experiment is a proof of the power and scalability of the bolometric technique to the ton scale. Recent developments in scintillating crystals demonstrate the technology for a future zero-background search [19, 53, 54, 70, 71]. These advances will be exploited in the next generation bolometric experiment, CUPID [71], which will reuse the CUORE cryostat and infrastructure.

ACKNOWLEDGMENTS

The data presented here can be made available upon reasonable request.

---

^a Corresponding author: cuore-spokesperson@lngs.infn.it
^b Deceased

[1] G. Racah, Nuovo Cimento **14**, 322 (1937).
[2] W. H. Furry, Phys. Rev. **56**, 1184 (1939).
[3] B. Pontecorvo, Sov. Phys. JETP **26**, 984 (1968).
[4] J. Schechter and J. W. F. Valle, Phys. Rev. **D25**, 2951 (1982).
[5] M. Fukugita and T. Yanagida, Phys. Lett. B **174**, 45 (1986).
[6] P. Minkowski, Phys. Lett. **67B**, 421 (1977).
[7] G. Prezeau, M. Ramsey-Musolf, and P. Vogel, Phys. Rev. **D68**, 034016 (2003).
[8] A. Atre et al., JHEP **05**, 030 (2009).
[9] M. Blennow et al., JHEP **07**, 096 (2010).
[10] F. Bonnet et al., JHEP **03**, 055 (2013), [Erratum: JHEP04,090(2014)].
[11] M. Mitra, G. Senjanovic, and F. Vissani, Nucl. Phys. **B856**, 26 (2012).
[12] V. Cirigliano et al., JHEP **12**, 082 (2017).
[13] V. Cirigliano et al., JHEP **12**, 097 (2018).
[14] M. Agostini, G. Benato, and J. Detwiler, Phys. Rev. **D96**, 053001 (2017).
[15] M. Agostini et al. (GERDA), Science **365**, 1445 (2019).
[16] S. I. Alvis et al. (Majorana), Phys. Rev. **C100**, 025501 (2019).
[17] G. Anton et al. (EXO-200), Phys. Rev. Lett. **123**, 161802 (2019).
[18] A. Gando et al. (KamLAND-Zen), Phys. Rev. Lett. **117**, 082503 (2016), [Addendum: Phys. Rev. Lett.117,no.10,109903(2016)].
[19] O. Azzolini et al. (CUPID-0), Phys. Rev. Lett. **123**, 032501 (2019).
[20] C. Arnaboldi et al. (CUORE), Nucl. Instrum. Meth. **A518**, 775 (2004).
[21] C. Brofferio, O. Cremonesi, and S. Dell'Oro, Front.in Phys. **7**, 86 (2019).
[22] E. Fiorini and T. Niinikoski, Nucl. Instrum. Meth. **224**, 83 (1984).
[23] C. Enss and D. McCammon, J. Low Temp. Phys. **151**, 5 (2008).
[24] C. Arnaboldi et al., J. Cryst. Growth **312**, 2999 (2010).
[25] M. Redshaw et al., Phys. Rev. Lett. **102**, 212502 (2009).
[26] N. D. Scielzo et al., Phys. Rev. C **80**, 025501 (2009).
[27] S. Rahaman et al., Phys. Lett. B **703**, 412 (2011).
[28] M. A. Fehr, M. Rehkämper, and A. N. Halliday, International Journal of Mass Spectrometry **232**, 83 (2004).
[29] C. Alduino et al. (CUORE), Int. J. Mod. Phys. **A33**, 1843002 (2018).
[30] C. Brofferio and S. Dell'Oro, Rev. Sci. Instrum. **89**, 121502 (2018).
[31] C. Alduino et al. (CUORE), JINST **11**, P07009 (2016).
[32] E. Andreotti et al., Astropart. Phys. **34**, 822 (2011).
[33] K. Alfonso et al. (CUORE), Phys. Rev. Lett. **115**, 102502 (2015).
[34] E. E. Haller et al., in Neutron Transmutation Doping of Semiconductor Materials, edited by R. D. Larrabee (Springer US, Boston, MA, 1984) pp. 21–36.
[35] A. Alessandrello et al., Nucl. Instrum. Meth. **A412**, 454 (1998).
[36] E. Andreotti et al., Nucl. Instrum. Meth. **A664**, 161 (2012).
[37] C. Alduino et al., Cryogenics **102**, 9 (2019).
[38] F. Alessandria et al., Nucl. Instrum. Meth. **A727**, 65 (2013).
[39] E. Buccheri et al., Nucl. Instrum. Meth. A **768**, 130 (2014).
[40] C. Arnaboldi et al., JINST **13**, P02026 (2018).
[41] S. Di Domizio et al., JINST **13**, P12003 (2018).
[42] G. Benato et al., JINST **13**, P01010 (2018).
[43] A. D'Addabbo et al., Cryogenics **93**, 56 (2018).
[44] C. Alduino et al. (CUORE), Phys. Rev. Lett. **120**, 132501 (2018).
[45] J. S. Cushman et al., Nucl. Instrum. Meth. A **844**, 32 (2017).
[46] E. Gatti and P. F. Manfredi, Riv. Nuovo Cim. **9N1**, 1 (1986).
[47] S. Di Domizio, F. Orio, and M. Vignati, JINST **6**, P02007 (2011).
[48] K. Alfonso et al., JINST **13**, P02029 (2018).
[49] C. Alduino et al. (CUORE), Phys. Rev. C **93**, 045503 (2016).
[50] P. C. Mahalanobis, Proc. Natl. Inst. Sci. India , 49 (1936).
[51] A. Drobizhev, Searching for the $0\nu\beta\beta$ decay of ^{130}Te with the ton-scale CUORE bolometer array, Ph.D. thesis, University of California, Berkeley (2018).
[52] L. Marini, The CUORE experiment: from the commissioning to the first $0\nu\beta\beta$ limit, Ph.D. thesis, Università degli Studi di Genova (2018).
[53] C. Alduino et al. (CUORE), Eur. Phys. J. **C77**, 543 (2017).
[54] C. Alduino et al. (CUORE), Eur. Phys. J. **C77**, 13 (2017).
[55] A. Caldwell, D. Kollár, and K. Kröninger, Computer Physics Communications **180**, 21972209 (2009).
[56] J. Kotila and F. Iachello, Phys. Rev. **C85**, 034316 (2012).
[57] J. Engel and J. Menéndez, Rept. Prog. Phys. **80**, 046301 (2017).
[58] J. Barea, J. Kotila, and F. Iachello, Phys. Rev. **C91**, 034304 (2015).

[59] F. Šimkovic *et al.*, Phys. Rev. **C87**, 045501 (2013).

[60] J. Hyvärinen and J. Suhonen, Phys. Rev. **C91**, 024613 (2015).

[61] J. Menéndez *et al.*, Nucl. Phys. **A818**, 139 (2009).

[62] T. R. Rodriguez and G. Martinez-Pinedo, Phys. Rev. Lett. **105**, 252503 (2010).

[63] N. López Vaquero, T. R. Rodríguez, and J. L. Egido, Phys. Rev. Lett. **111**, 142501 (2013).

[64] J. M. Yao *et al.*, Phys. Rev. **C91**, 024316 (2015).

[65] M. T. Mustonen and J. Engel, Phys. Rev. **C87**, 064302 (2013).

[66] A. Neacsu and M. Horoi, Phys. Rev. **C91**, 024309 (2015).

[67] A. Meroni, S. T. Petcov, and F. Simkovic, JHEP **02**, 025 (2013).

[68] V. Cirigliano *et al.*, Phys. Rev. Lett. **120**, 202001 (2018).

[69] V. Cirigliano *et al.*, Phys. Rev. **C100**, 055504 (2019).

[70] E. Armengaud *et al.* (CUPID-Mo), (2019), arXiv:1909.02994 [physics.ins-det].

[71] W. R. Armstrong *et al.* (CUPID), (2019), arXiv:1907.09376 [physics.ins-det].